Journal of
Synchrotron
Radiation

ISSN 0909-0495

Received 18 January 2010
Accepted 9 April 2010

Detective quantum efficiency, modulation transfer function and energy resolution comparison between CdTe and silicon sensors bump-bonded to XPAD3S

Kadda Medjoubi,[a]* Thierry Bucaille,[a] Stéphanie Hustache,[a] Jean-François Bérar,[b] Nathalie Boudet,[b] Jean-Claude Clemens,[c] Pierre Delpierre[c] and Bernard Dinkespiler[c]

[a]Synchrotron SOLEIL, France, [b]D2AM-CRG/F, France, and [c]CPPM-IN2P3, France.
E-mail: kadda.medjoubi@synchrotron-soleil.fr

XPAD3S is a single-photon-counting chip developed in collaboration by SOLEIL Synchrotron, the Institut Louis Néel and the Centre de Physique de Particules de Marseille. The circuit, designed in the 0.25 μm IBM technology, contains 9600 square pixels with 130 μm side giving a total size of 1 cm × 1.5 cm. The main features of each pixel are: single threshold adjustable from 4.5 keV up to 35 keV, 2 ms frame rate, 10^7 photons s^{-1} mm^{-2} maximum local count rate, and a 12-bit internal counter with overflow allowing a full 27-bit dynamic range to be reached. The XPAD3S was hybridized using the flip-chip technology with both a 500 μm silicon sensor and a 700 μm CdTe sensor with Schottky contacts. Imaging performances of both detectors were evaluated using X-rays from 6 keV up to 35 keV. The detective quantum efficiency at zero line-pairs mm^{-1} for a silicon sensor follows the absorption law whereas for CdTe a strong deficit at low photon energy, produced by an inefficient entrance layer, is measured. The modulation transfer function was evaluated and it was shown that both detectors present an ideal modulation transfer function at 26 keV, limited only by the pixel size. The influence of the Cd and Te *K*-edges of the CdTe sensor was measured and simulated, establishing that fluorescence photons reduce the contrast transfer at the Nyquist frequency from 60% to 40% which remains acceptable. The energy resolution was evaluated at 6% with silicon using 16 keV X-rays, and 8% with CdTe using 35 keV X-rays. A 7 cm × 12 cm XPAD3 imager, built with eight silicon modules (seven circuits per module) tiled together, was successfully used for X-ray diffraction experiments. A first result recently obtained with a new 2 cm × 3 cm CdTe imager is also presented.

Keywords: XPAD; CdTe sensor; silicon sensor; DQE; MTF.

1. Introduction

Third-generation synchrotron light sources deliver a very high brilliance beam, *i.e.* a high photon flux with a small divergence. These characteristics, combined with the recent advances in the field of detectors, open new perspectives for synchrotron science. Classical experiments can now be performed faster, with higher spatial resolution, and new studies, such as fast kinetics follow up, can be considered.

Designed initially for high-energy physics, the hybrid pixel detectors meet the specifications of many synchrotron experiments. These detectors consist of a sensor coupled with an electronic circuit. The rear face of the sensor is pixellated and each pixel is connected to a photon-counting readout electronic channel. Their high frame rate, noiseless and stable operation, energy discrimination capability, electronic shutter and very large dynamic range enable improvements to synchrotron experiments like protein crystallography (Brönnimann *et al.*, 2003), small-angle X-ray scattering (SAXS) (Ponchut *et al.*, 2005) and pump–probe measurements (Ejdrup *et al.*, 2009). The main existing developments, PILATUS (Henrich *et al.*, 2009), MEDIPIX2 (Ponchut *et al.*, 2007) and XPAD (Basolo *et al.*, 2007), are starting to be routinely used on synchrotron beamlines.

The most commonly used sensor for this kind of detector is a planar silicon diode. This material has the advantage of being very well known with regard to its physical properties and fabrication processes. On the other hand, owing to its

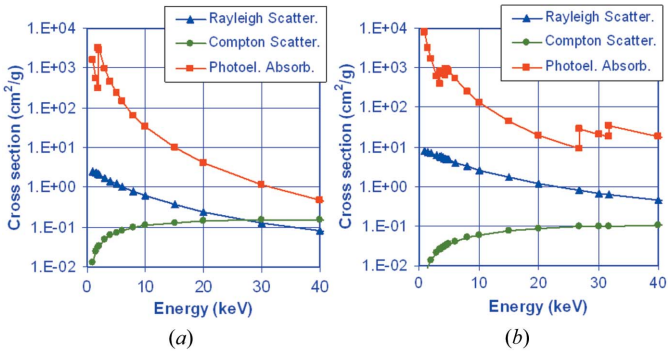

Figure 1
Compton, Rayleigh and photoelectric cross section for (*a*) Si and (*b*) CdTe (data from NIST-XCOM, http://physics.nist.gov/PhysRefData/Xcom/Text/XCOM.html).

low Z and consequently low detection efficiency, its use is, in practice, restricted to X-ray experiments below 25 keV, excluding a large part of material science experiments and hard X-ray imaging. Therefore, high-Z sensors, such as CdTe, CZT or GaAs, are being investigated (Basolo *et al.*, 2008; Fröjdh *et al.*, 2006; Clajus *et al.*, 2006; Zwerger *et al.*, 2007). Fig. 1 illustrates the superior absorption efficiency of CdTe in the high-energy range compared with Si.

In this paper we present a comparative study of the imaging performances of the XPAD3 chip bump-bonded to a Si or a CdTe sensor. The XPAD3 circuit was designed for synchrotron and medical imaging applications within the framework of the XPIX collaboration (SOLEIL, Institut Louis Néel and Centre de Physique des Particules de Marseille). Diffraction experiments and imaging tests have been successfully performed and are presented by Basolo *et al.* (2008) and Berar *et al.* (2009). Cassol-Brunner *et al.* (2009) quantified the modulation transfer function (MTF) and detective quantum efficiency (DQE) under the experimental conditions of small-animal imaging in the laboratory, with polychromatic incident radiation from a filtered molybdenum X-ray tube. In this paper these quantities are measured for synchrotron applications, with monochromatic radiation. Comparison was made from 6 keV up to 35 keV. In the case of CdTe, measurements were also realised around the K-absorption edges of Cd (26.7 keV) and Te (31.8 keV) in order to quantify their effects on the detector performances.

The measurements were performed on SOLEIL beamlines (DIFFABS, PROXIMA 1 and CRISTAL) and on the ESRF CRG beamline (D2AM).

2. Detector description

2.1. The XPAD3S circuit

XPAD3S is the third generation of a photon-counting circuit designed by the CPPM. Previous versions have been presented and evaluated by Delpierre *et al.* (2007). This new circuit, manufactured in the 0.25 µm IBM technology, consists of 9600 square pixels with 130 µm side. The pixellated area covers 1 cm × 1.5 cm. Each pixel contains a complete independent photon-counting readout electronic, composed of a pre-amplifier, an operational transconductance amplifier, a discriminator with single threshold and a counter (Pangaud *et al.*, 2008). The input polarity of the chip is positive, this version being dedicated to collecting 'holes'. The shaping time of the preamplifier is tunable down to 150 ns, for a maximum count rate close to 1 MHz with less than 10% dead-time losses. The single threshold is adjustable from 4.5 keV up to 35 keV (for a silicon sensor) with a dispersion of typically 200 eV (r.m.s.). This relatively low resolution is caused by an unbalanced power consumption from the left to the right of the chip. This default is corrected in a second version of the chip (very recently manufactured but not tested at the time of submitting this paper) where the threshold step will be strongly reduced.

The pulse counting is performed on chip by a 12-bit counter with an overflow bit whose state can be scanned at high frequency without interrupting the counting process. This continuous reading and treatment of this overflow bit allows the image dynamic range to be increased virtually to infinity (27-bit in our actual case). Unfortunately, the readout 'on the fly' of the overflow bit induces noise which made this mode of operation unusable in the first version of the XPAD3S. For this reason it was decided to inhibit the pixel for 10 µs during each 2 ms for the overflow reading. This defect is corrected in the design of the second version of the chip.

At the end of an acquisition, the whole counter and overflows value for all pixels can be read in less than 2 ms before starting a new image.

In order to be able to match almost every experimental constraint, especially for medical imaging, a 'C' version of the XPAD3 has also been developed. With the same principal parameters as the XPAD3S, this circuit collects electrons instead of holes and has a windowed energy selection obtained with two thresholds, each one being adjustable from 6 up to 60 keV (Pangaud *et al.*, 2007). The large dispersion of the thresholds per pixel have, to date, made this circuit of limited use, but a new corrected 'C' version has been designed, recently manufactured and will be tested soon.

2.2. The sensors

Single and dual XPAD3S circuits were respectively flip-chip bonded to silicon and CdTe sensors (Basolo *et al.*, 2008).

2.2.1. Silicon sensors. The silicon sensor, manufactured by CiS (http://www.cismst.de/), consists of an array of silicon planar pn-junction photodiodes. It is made on a 1 cm × 1.5 cm high-resistivity n-type silicon bulk pixellated on one side (the cathode plane) with aluminized p+ implant. The size of the pads is 100 µm × 100 µm, with a pitch of 130 µm in both directions. The anode plane (entrance side of the sensor for the photons) is uniformly n+ doped and also aluminized. The sensor is 500 µm-thick and requires a 100 V reverse bias to be fully depleted. The dark current measured under these conditions is less than 1.5 nA per diode.

The hybridization of the circuit to the sensor is performed by IZM (http://www.izm.fraunhofer.de/) with Sn/Pb bump bonds.

Table 1
Charge mobility properties of Si and CdTe.

	Mobility ($cm^2\ V^{-1}\ s^{-1}$)		Lifetime (s)	
Sensor	Electron	Hole	Electron	Hole
Si	1400	480	$>10^{-3}$	2×10^{-3}
CdTe	1100	100	3×10^{-6}	2×10^{-6}

2.2.2. CdTe sensors. The sensor is a 700 µm-thick high-resistivity p-type CdTe from Acrorad (http://www.acrorad.co.jp/), with an active area of 1.5 cm × 2 cm, and the same pixel geometry as the silicon sensors. Since the input polarity of XPAD3S is positive, the CdTe sensor is used in the hole collection mode, which is not the most suitable for this material. Indeed, the low mobility and the short lifetime of holes in CdTe (*cf.* Table 1) owing to charge trapping can strongly reduce the charge collection efficiency (CCE). In order to prevent this loss and make the amount of collected charge independent of the depth of the photon interaction, a high bias voltage is required. The leakage current has therefore to be limited thanks to a Schottky Ti(∼30 nm)/In(∼300 nm)/CdTe contact on the anode plane. Another advantage of these Schottky barriers with respect to ohmic contacts is a significant improvement in the energy resolution, as reported by Matsumoto *et al.* (1998).

The pixel side contacts are near ohmic type Pt(∼200–300 nm)/CdTe contacts. The hybridization is performed by Ajat (http://www.ajat.fi/) with Sn/Bi bump bonds. This eutectic mixture was selected for its low melting point (412 K) (Bigas *et al.*, 2007) in order to have a low-temperature processing and therefore to prevent any damage to the CdTe sensor.

A first characterization of the sensor was carried out previously (Basolo *et al.*, 2008), where it was shown that, with a ^{241}Am source, a good CCE could be reached at 900 V bias with a stable reverse current as low as 5 pA per diode at room temperature. As expected with Schottky contacts, a polarization phenomenon (Toyama *et al.*, 2006) was observed. This effect gradually degrades the CCE during X-ray illumination. A sequence of switching off and on the bias voltage (5 s reset every 10 min) was successfully used to restore the initial value of the CCE. The same bias and sequence are employed in the present study.

2.2.3. Evaluation board. The single and dual chip, hybridized with Si and CdTe, respectively, are mounted on printed circuit boards dedicated to evaluation tests (Fig. 2). The control and readout of the chip are performed by an FPGA (ALTERA DE2, http://www.altera.com/) which is connected *via* TCP/IP to a computer which runs the data acquisition software.

3. MTF measurements

The modulation transfer function is widely used to characterize the spatial resolution of a two-dimensional imaging system. It describes the transfer of the incident contrast through the detector for any spatial frequency. The MTF is defined as the modulus of the Fourier transform of the two-dimensional point-spread function (PSF). The PSF is the detector response to an incident narrow pencil beam. For an isotropic spatial response, the MTF is a one-dimensional function (Dainty & Shaw, 1974) obtained from the modulus of the Fourier transform of the line-spread function (LSF), *i.e.* the projection of the PSF along one direction.

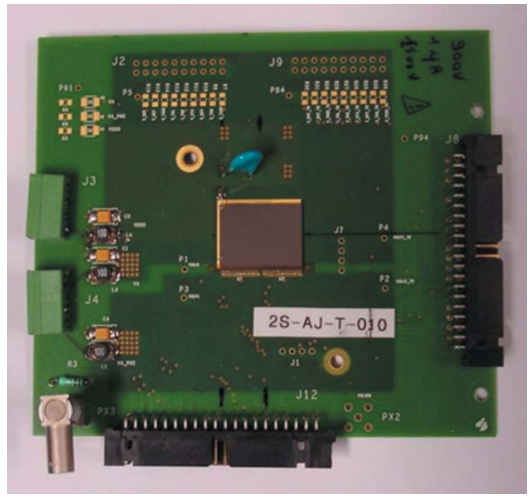

Figure 2
Dual circuits hybridized with single CdTe mounted on a printed circuit board.

3.1. Physical processes

Different physical processes taking place in a solid-state X-ray converter, such as spatial extension of the primary charge cloud, fluorescence emission and Compton/Rayleigh scattering, can affect the PSF and therefore the MTF.

The absorption of the incident X-ray by the photoelectric effect in a given atomic shell (K, L, M, ...) produces a photoelectron and, according to the fluorescence yield, either an Auger electron or a photon fluorescence. Photoelectrons and Auger electrons are charged particles and they create, close to the primary interaction point, a quantity of charge equal to their energy divided by the energy needed for an electron–hole pair creation [3.6 eV in Si and 4.43 eV in CdTe (Spieler, 2008)]. Up to 40 keV, the initial extension of the charge cloud, given by the primary electron range and calculated using Katz–Penfold's formula (Katz & Penfold, 1952), is less than 11 µm and 4 µm in Si and CdTe, respectively. Electrons and holes drift along the vertical electric field toward the anode and the cathode, respectively. During the drift, owing to diffusion, the charge cloud spreads out spatially. For a charge generated close to the anode and for a constant electric field, the standard deviation of the charge distribution on the pixel side (cathode), assumed to be Gaussian, is written as (Spieler, 2008)

$$\sigma = \left[2\left(\frac{kT}{q}\right)\frac{t^2}{V_\mathrm{b}}\right]^{1/2}, \qquad (1)$$

where kT/q = 26 mV at room temperature, t is the sensor thickness and V_b is the bias voltage.

Considering the parameters given in §2.2.2 (sensor thickness and bias voltage), the expected extensions (r.m.s.) owing to diffusion during charge drift in Si and CdTe are 11 µm and 5 µm, respectively.

In the worse case, a 40 keV photon can produce, close to the entrance side, a photoelectron whose emission is parallel to the electrode. Thus, the final charge cloud extension is given by the convolution of the electron range and of the lateral diffusion and will be less than 12 µm (r.m.s.) on the pixel side in both sensors. Even if this value is low compared with the pixel size, if a photon is converted close to or on the border of a pixel the charge will be shared between neighbouring pixels, and the incoming photon can be counted twice. In order to avoid this double counting induced by charge sharing, the threshold has to be adjusted to half of the incident photon energy (Broennimann *et al.*, 2006). If this condition is met, the influence of the charge cloud extension on the PSF should be negligible.

When a Compton or Rayleigh effect occurs, the scattered photon may travel a long distance from the primary interaction point before being absorbed by the photoelectric effect. In CdTe and Si, from a few keV up to 40 keV, the probability that the first X-ray interaction in the sensor is a Compton or Rayleigh scattering is low compared with the photoelectric effect. Indeed, as shown in Fig. 1, the cross sections for Compton and Rayleigh scattering are, at least, around one order of magnitude lower than for the photoelectric effect. These processes therefore do not contribute significantly to the degradation of the PSF.

Fluorescence photons, emitted isotropically, may travel a large distance away from the primary interaction point before being converted to charged particles (Auger or photoelectron). This effect contributes to broaden the PSF if this distance is large compared with the pixel size.

This is not the case for the $K\alpha$ fluorescence in Si (1.7 keV), whose mean free path is only a few micrometres, to be compared with 130 µm in the case of XPAD3.

On the other hand, energies of $K\alpha$ fluorescence from Cd and Te are 23.17 keV and 27.47 keV with mean free paths in CdTe of 110 µm and 60 µm, respectively (the mean free path of Te $K\alpha$ fluorescence being reduced because its energy is above the *K*-edge of Cd). The spatial information in XPAD3 can therefore be altered by the excitation of the fluorescence of the sensor and this effect has to be quantified. $L\alpha$ fluorescence emissions from Cd and Te are less than 4 keV. Their mean free path in CdTe is less than 3 µm and they do not alter the PSF compared with $K\alpha$.

3.2. Analytical approach of the spatial response broadening in the CdTe sensor

According to the physical considerations listed above, the largest contribution to the broadening of the PSF should be induced by *K*-fluorescence of CdTe. A simple analytical model for CdTe is proposed below in order to predict the resulting effect on the spatial response of the detector.

Table 2
Probabilities of local (*a*) and shifted (*b*, *c*, *d*) events.

Energy	*a*	*b*	*c*	*d*
27 keV	42%	58%	0%	0%
32 keV	28%	34%	15%	23%

In this model, Compton and Rayleigh scattering, charge diffusion, charge sharing and charge trapping are not taken into account. The mean free path of *L*-fluorescence and the range of photoelectrons are considered to be nil.

As shown in Fig. 3, if the incident photon energy is just above the *K*-edge of Te, four cases have to be considered. Firstly, the incident photon is locally absorbed after photoelectric absorption. Secondly, the incident photon induces *K*-fluorescence from Cd or Te which is reabsorbed far from the primary interaction. The event is 'shifted once'. Thirdly, the incident photon induces *K*-fluorescence from Te which in turn induces *K*-fluorescence from Cd. In this case the event is 'shifted twice'. Finally, the fluorescence induced by the incoming photon can escape from the sensor.

The probability of each process (except the escape of fluorescence, because geometrical considerations have to be taken into account) can be deduced from the X-ray interaction diagram shown in Fig. 4. The probability of each elementary process is calculated according to the NIST X-ray database (http://physics.nist.gov/PhysRefData/Xcom/Text/XCOM.html). The diagram contains four regions corresponding to one of the cases listed above. Associated probabilities, depending on the incident X-ray energy, are noted *a*, *b*, *c* and *d* and listed in Table 2.

The spatial extension produced by the *K*-fluorescence from Te or Cd can be modelled by an analytical function. In this model the incoming pencil beam impinges perpendicularly to the infinite surface of the sensor, at coordinates $x = 0$ and $y = 0$. The three-dimensional distribution of the fluorescence photons of energy $E_{\rm fluo}$ generated at the depth z_0 and then absorbed at point (x,y,z) is calculated from the product of the following probabilities:

(i) Probability for the incident photon to be absorbed at z_0;

(ii) Probability for the generated fluorescence to be emitted along an angular direction (isotropic distribution);

(iii) Probability for the fluorescence photon to be absorbed at the distance $[x^2 + y^2 + (z - z_0)^2]^{1/2}$ from its point of emission.

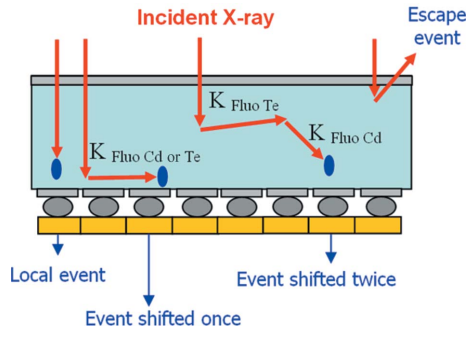

Figure 3
X-ray fluorescence processes in CdTe.

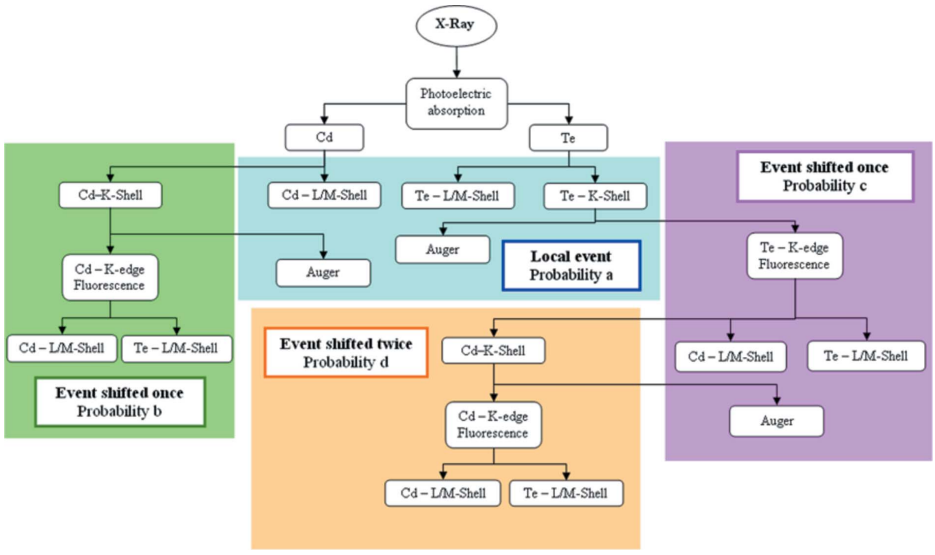

Figure 4
X-ray interaction diagram in CdTe.

The product is then integrated along the depth of the sensor (assumed isotropic) and is written as follows,

$$\frac{\mathrm{d}N(x, y, z, E, E_{\mathrm{fluo}})}{\mathrm{d}V} = \int_0^t \frac{1}{4\pi} \frac{\mu(E_{\mathrm{fluo}}) \exp\left\{-\mu(E_{\mathrm{fluo}})\left[x^2 + y^2 + (z - z_0)^2\right]^{1/2}\right\}}{x^2 + y^2 + (z - z_0)^2} \times \mu(E) \exp\left[-\mu(E) z_0\right] \mathrm{d}z_0, \quad (2)$$

with t the sensor thickness, E the energy of incident photons, E_{fluo} the energy of the K-fluorescence and μ the attenuation coefficient of CdTe.

The projection of expression (2) on the x axis gives the LSF produced by fluorescence along this direction.

Let $\mathrm{LSF}_{26\mathrm{keV}}(x)$ be the LSF measured at E = 26 keV, just below the Cd K-edge, with no contribution of the fluorescence of the sensor. The LSF at the vicinity of the Cd and Te K-edges is given by the following formula,

$$\begin{aligned}\mathrm{LSF}(x, E) = a(E)\ \mathrm{LSF}_{26\mathrm{keV}}(x) &+ b(E)\left[\mathrm{LSF}_{26\mathrm{keV}} \otimes N\left(x, E_{\mathrm{Fluo-Cd}}\right)\right] \\ &+ c(E)\left[\mathrm{LSF}_{26\mathrm{keV}} \otimes N(x, E_{\mathrm{Fluo-Te}})\right] \\ &+ d(E)\left[\mathrm{LSF}_{26\mathrm{keV}} \otimes N(x, E_{\mathrm{Fluo-Te}}) \otimes N\left(x, E_{\mathrm{Fluo-Cd}}\right)\right], \quad (3)\end{aligned}$$

with E the incident X-ray energy, $E_{\mathrm{Fluo\text{-}Cd}}$ the K-fluorescence photon average energy from Cd, $E_{\mathrm{Fluo\text{-}Te}}$ the K-fluorescence photon average energy from Te, and a, b, c and d the probabilities listed in this section.

3.3. Experimental set-up

In order to measure the PSF with a resolution better than the pixel pitch, 130 µm in our case, the PSF can be oversampled by recording the spatial response of a highly collimated incident beam for different positions along a pixel axis. The distance between two consecutive positions is chosen to be very small compared with the pixel size and was set to 10 µm in this study. The associated LSF is then deduced from a one-dimensional projection of the oversampled PSF.

The detector was mounted on a two-dimensional translation stage in order to be moved in the plane perpendicular to the X-ray beam, with 1 µm resolution (Bérar *et al.*, 2002). The beam was collimated down to 10 µm × 10 µm by slits located 10 cm upstream from the detector. In order to centre the beam in a single pixel, the detector was at first translated along both directions until a two-dimensional symmetric spatial response was obtained.

3.4. Results

The LSF is measured as described in §3.3. The following measurements were carried out with an energy threshold set at 14 keV. Fig. 5(*a*) presents the normalized LSF along one direction measured on Si and CdTe sensors at 26 keV. As shown, the LSFs are very similar and have a square shape very close to the perfect square pixel response with a 130 µm width.

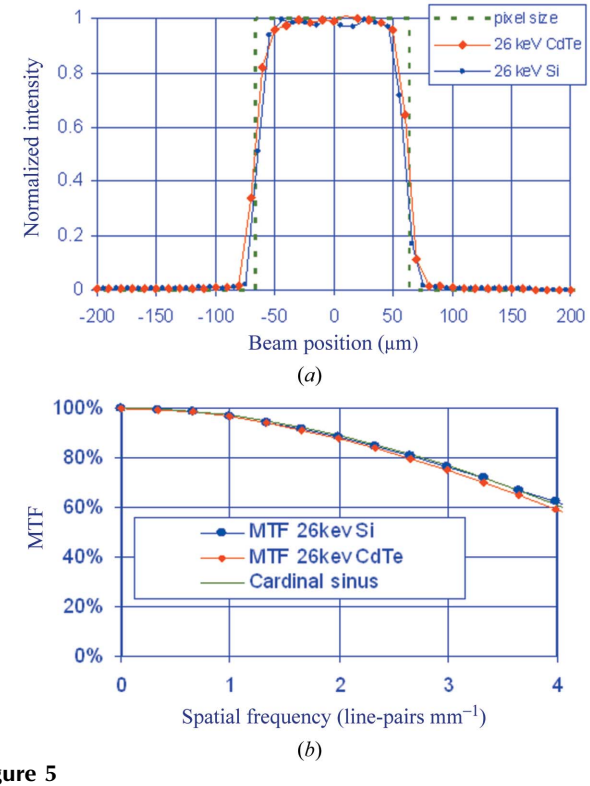

Figure 5
(*a*) LSF along one pixel direction measured on Si and CdTe at 26 keV. (*b*) MTF calculated from the LSF profile and compared with the theoretical curve.

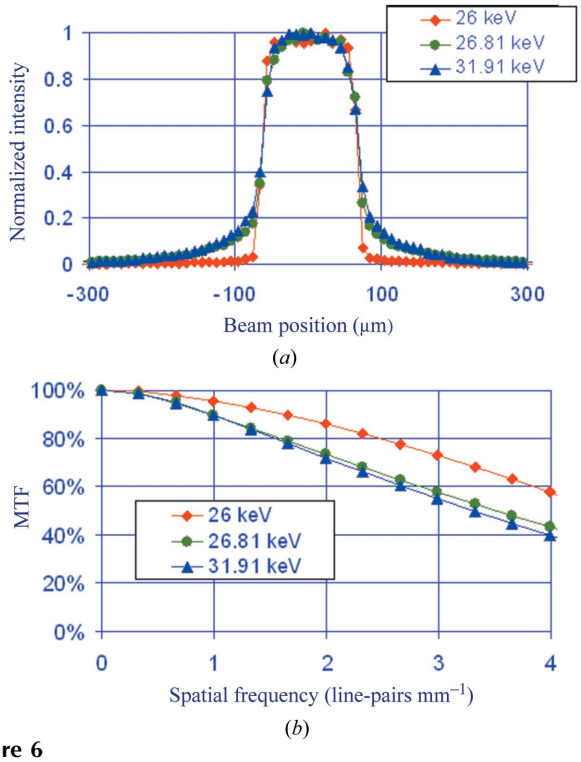

Figure 6
(*a*) LSF along one direction measured on CdTe at 26 keV, 26.81 keV and 31.91 keV. (*b*) MTF calculated from the LSF.

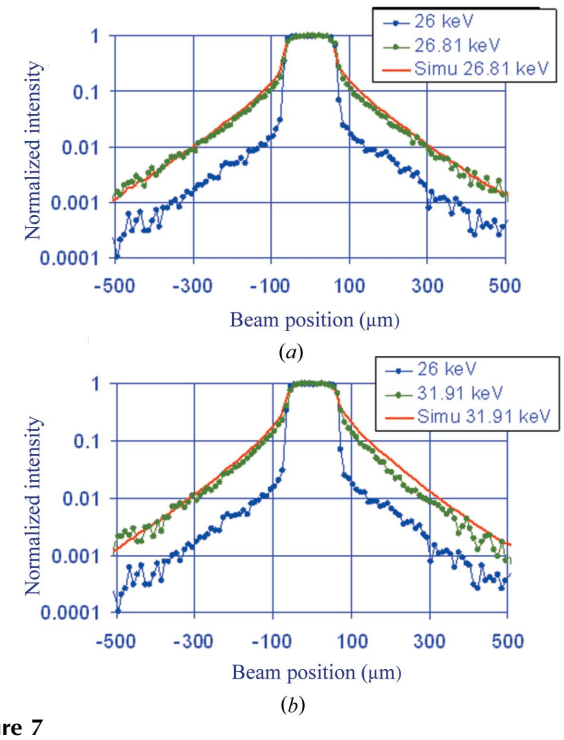

Figure 7
Comparison on CdTe between the measured LSF at (*a*) 26.81 keV and (*b*) 31.91 keV and the corresponding LSF obtained with the analytical model.

This means that the charge-sharing effect is suppressed when the threshold is more than half of the incident photon energy.

The corresponding modulation transfer functions are shown in Fig. 5(*b*). The Si and CdTe MTFs are similar and compare well with the theoretical cardinal sinus curve.

Fig. 6 presents the LSF and MTF measurement on CdTe at 26 keV (below the Cd *K*-edge), 26.81 keV (above the Cd *K*-edge and below the Te *K*-edge) and 31.91 keV (above the Te *K*-edge). As shown, above the Cd *K*-edge and the Te *K*-edge a similar long-range tail, produced by fluorescence emission, is observed. This effect decreases the MTF from 60% to 40% at the Nyquist frequency indicating that, with this pixel size, operation above *K*-edges of CdTe still gives satisfactory results.

The analytical model, presented in §3.2, is used to simulate the LSF above the CdTe *K*-edges. The results are shown and compared with data in Fig. 7. The agreement is good and proves that the spatial extension is mainly produced by fluorescence emission in CdTe.

4. Spectral performances

The ability of a detector to measure the energy of an incident photon is defined by its energy resolution. This important parameter is measured by exposing the detector to monochromatic radiation and observing the resulting energy spectrum. The resolution is then given by the full width at half-maximum of the peak corresponding to the incident photon energy. This width is caused by Fano broadening, electronic noise and collection efficiency (charge trapping, charge sharing). In a pixel detector, where the spectrum is obtained by differentiation of the single threshold scan (S-curve), if the energy measurement has to be carried out on a cluster of pixels the pixel threshold dispersion will also broaden the measured energy resolution.

4.1. Spectral measurements

Spectral measurements were carried out on Si and CdTe at 16 keV and 35 keV, respectively (Fig. 8). In both cases the detectors were exposed to a flat-field illumination obtained by scattering X-rays from a few millimetres of glass. Each spectrum was obtained by differentiation of the average of several very similar S-curves (*i.e.* with the same threshold dispersion) in order to reduce the statistical noise. It has to be noted that the calibration used to reduce the inter-pixel threshold dispersion was performed for each chip at $E/2$ which is not ideal for energy resolution measurement at E.

The Si sensor exhibits an energy resolution of about 1 keV at 16 keV corresponding to an energy resolution ($\Delta E/E$) of 6%. The peak-to-valley ratio owing to the charge sharing is about 4. Below half of 16 keV, the number of counts increases owing to the increase in the multiplicity (number of measured counts per photon absorbed).

The spectrum obtained with CdTe at 35 keV contains several peaks. The photopeak is clearly defined which proves that, even in hole collection mode, a good charge collection efficiency can be achieved if a high bias voltage is applied. Indeed, according to the Hecht equation (Spieler, 2008) (assuming a uniform internal electric field and charge trapping distributed uniformly within the sensor) and parameters listed

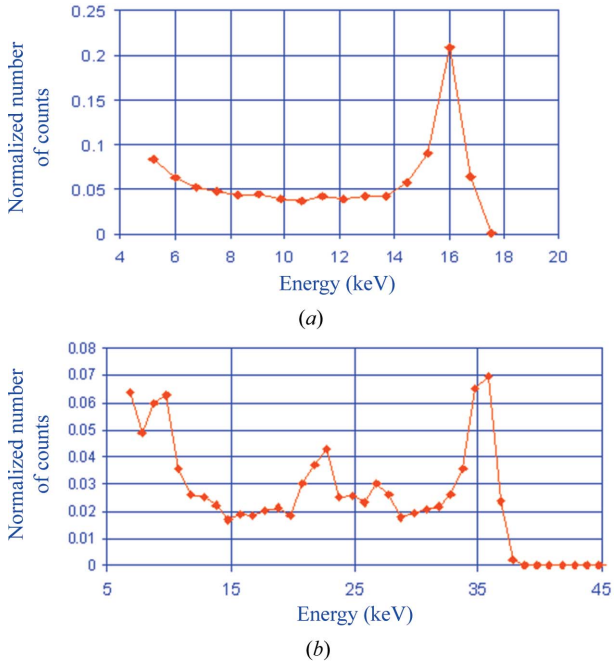

Figure 8
Spectral measurement on (*a*) Si and (*b*) CdTe exposed to a 16 keV and 35 keV flat field, respectively.

in Table 1, the CCE is evaluated to be 98% for a 900 V bias. The width of the photopeak is about 3 keV corresponding to an energy resolution of 8%. *K*-fluorescence peaks from Cd and Te are clearly visible. Some fluorescence events are therefore detected independently on a single pixel. The peak-to-valley ratio (∼3.5) is lower than in Si possibly due to the contribution of the fluorescence peaks. Below 15 keV, as was observed for Si, the increase in the multiplicity increases the number of counts. The escape peak from Te is also visible around 9 keV.

4.2. Influence of bias voltage on the spectral performance of the CdTe sensor

This experiment was performed with a copper anode X-ray tube on the CdTe detector. An 8 keV monochromatic beam was produced using a germanium crystal. This beam was then collimated down to a 50 µm diameter. By the method explained in §3.2, a single pixel was exposed. Fig. 9 presents two spectra obtained at 900 V and 1900 V bias voltage. The number of counts in the photopeak increases by a factor of 1.9 between these two spectra without any change of the peak position. This implies that at 900 V the low-energy photons (such as the 8 keV photons employed in this experiment) which are absorbed close to the anode (mean free path in CdTe ∼6 µm) are not completely collected. The CCE of 98% calculated in §4 does not explain this effect and this suggests the existence of a not fully efficient layer below the anode.

In order to evaluate the maximum bias voltage that can be applied on this CdTe sensor, a measurement of the total reverse current up to the breakdown voltage was performed (Fig. 10). The breakdown appears at 2300 V and does not seriously damage the sensor. Indeed, at lower voltage the

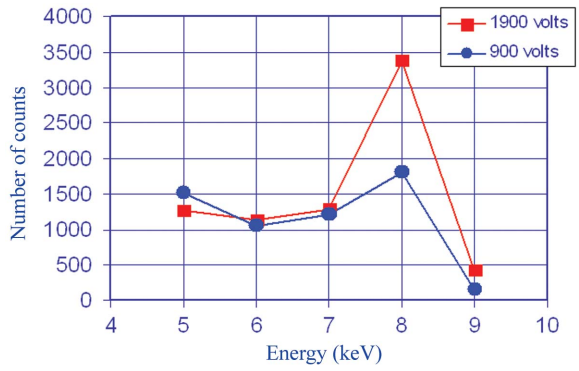

Figure 9
8 keV spectra measured on CdTe at 900 V and 1900 V bias voltage.

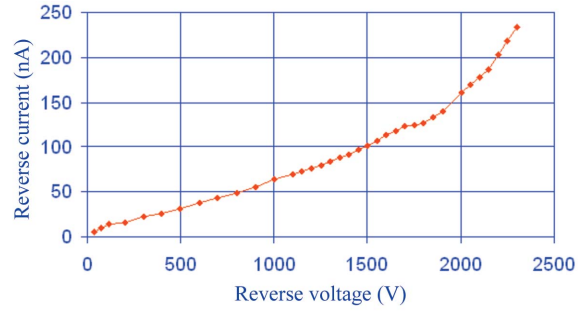

Figure 10
Reverse current *versus* bias voltage on CdTe sensor.

detector seems to work as previously except with a slight increasing of the reverse current.

5. DQE measurement

The DQE describes the transfer of the square of the signal-to-noise ratio through an imaging system. If the incident noise is Poisson distributed, the DQE is written as follows (Ponchut, 2006),

$$\mathrm{DQE}(\nu) = G \times \mathrm{MTF}^2(\nu) \times \frac{\bar{S}}{\mathrm{NPS}(\nu)}, \qquad (4)$$

where G is the detector conversion factor (output signal per incident X-ray), $\bar{S}$ is the average signal in a region of interest (ROI) and NPS is the noise power spectrum calculated in this ROI.

At zero frequency, the DQE describes the transfer of the flat quanta image through an imaging system. The DQE (0 line-pairs mm^{-1}) was measured from 6 keV up to 35 keV for the Si and CdTe detectors.

5.1. Noise power spectrum

The noise power spectrum (NPS) corresponds to the spectral decomposition of the variance as a function of the spatial frequency. It is evaluated by Fourier analysis on flat-field images (Dainty & Shaw, 1974; Ponchut, 2006) which were obtained in this work by scattered X-rays from a few millimetres of glass, water or carbon (depending on the beam energy). In order to quantify only the stochastic noise, the

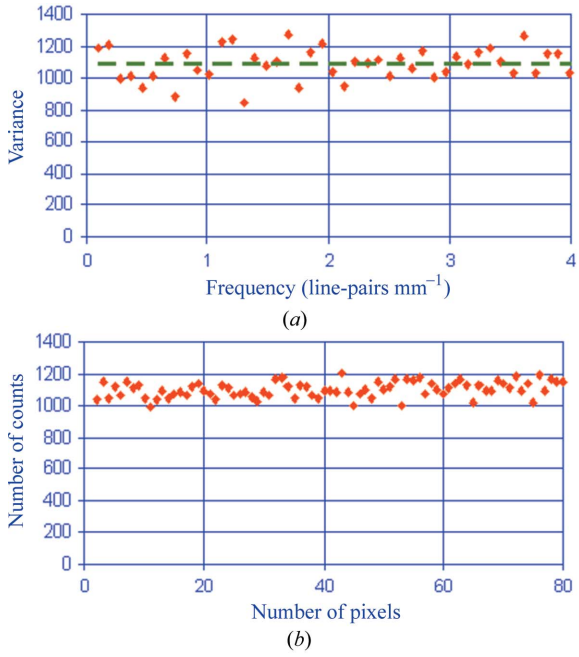

Figure 11
(*a*) NPS and (*b*) average profile measured on a ROI at 27 keV with threshold at 14 keV on CdTe.

image used to calculate the NPS was corrected from the fixed pattern noise by subtracting by the average of 100 similar flat-field images.

Fig. 11(*a*) presents the one-dimensional NPS obtained with the CdTe detector at 27 keV with the threshold adjusted for 14 keV at close to half of beam energy. The measurement was carried out in a ROI of 80 × 30 pixels without any dead pixels. Although noisy, it appears clearly that the NPS is white. This result indicates that pixels are uncorrelated.

Fig. 11(*b*) presents the projection of the ROI along one direction. The average number of counts per pixel is about 1100 which is equivalent to the NPS value. The same measurement was performed on both detectors for different energies and has confirmed that the stochastic noise is mainly quantum noise.

Therefore, as expected, for a pixel detector and a monochromatic beam, the DQE (0 line-pairs mm^{-1}) is reduced to the detector efficiency if the threshold of all pixels is adjusted to half of the photon incident energy.

5.2. DQE (0 line-pairs mm^{-1})

The DQE at zero frequency (or detector efficiency) was evaluated by using the detector gain measurement method described by Ponchut (2006). An aperture (∼2 mm^2), limited by two pairs of slits placed close to the detector, was exposed to a flat-field illumination produced as for the NPS measurements. Images were taken with the threshold per pixel adjusted to half of the beam energy. The number of counts per pixel integrated within this aperture was compared with the number of X-rays passing through the slits (the latter measurement being made using a $LaBr_3$ scintillator coupled to a photomultiplier tube).

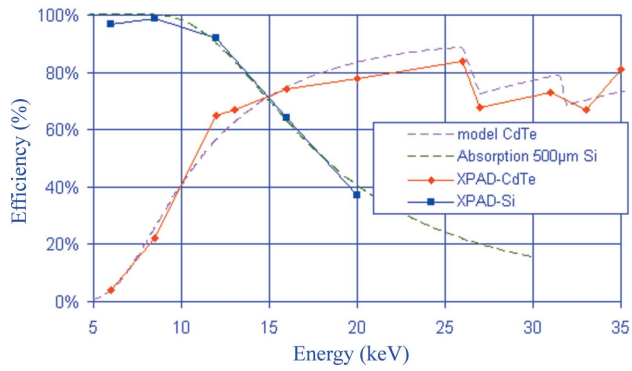

Figure 12
DQE (0 line-pairs mm^{-1}) measured on Si- and CdTe-XPAD3S and compared with models.

Fig. 12 shows the DQE at zero spatial frequency measured on Si and CdTe from 6 keV up to 35 keV. The detection efficiency in Si follows the absorption law, whereas in CdTe we observed a strong deficit at low photon energy which is not explained by the anode contact absorption (5% at 8 keV). As discussed in §4, this indicates that an amount of charge created close to the anode side is not collected at 900 V. Therefore, as was observed in §4, this suggests the existence of an inefficient layer below the anode contact.

The inefficient layer, considered as a dead layer, was investigated by using the method already applied to determine the inactive thickness of CdTe sensors by Zahraman *et al.* (2006). Indeed, the detector was exposed to a narrow 8 keV beam from an X-ray tube and images were acquired for various incident angles to the normal of the sensor surface. Fig. 13 shows the integral of the image normalized with the value obtained at 0° for different incident angles. The dead-layer thickness is estimated by fitting the data with the following expression,

$$\frac{N(\theta)}{N(0^\circ)} = \exp\left(-\mu_{\mathrm{CdTe}}\,\frac{t}{\cos\theta}\right), \qquad (5)$$

where N is the image integral, θ is the incident angle, μ_{CdTe} is the CdTe linear attenuation coefficient at 8 keV and t is the dead-layer thickness. As shown in Fig. 13, a good agreement is found using a dead thickness of 10 µm.

The theoretical efficiency is now calculated by considering the 10 µm dead layer. A simple analytical model was written

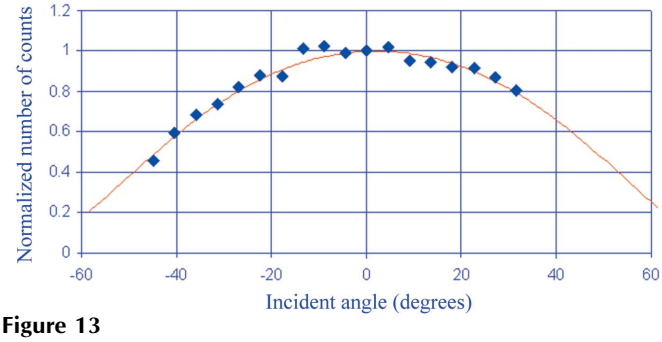

Figure 13
Image integral, as a function of the incident angle, normalized with the value obtained at 0° on the CdTe-XPAD3 at 8 keV.

and considers: (i) the dead layer absorption; (ii) the fluorescence emitted from the dead layer and absorbed in the active CdTe volume; (iii) the escape fluorescence from the active CdTe volume; (iv) a multiplicative factor equal to 0.95 which may be caused by the pixel fill factor.

The model, as can be seen in Fig. 12, is in good agreement with the data. It confirms the existence of an inefficient region below the anode contact. As explained by Zahraman *et al.* (2006), active defects can be introduced below the electrode by the metallization process used for contact deposition. An equivalent or related effect could explain this inefficiency observed in this work.

6. Si and CdTe imagers

Three 7 cm × 12 cm detectors with Si sensors have been constructed. The detectors are built with eight tiled modules. Each module is composed of seven XPAD3S circuits flip-chip bonded on a 1 cm × 7 cm pixellated silicon sensor (Fig. 14).

One of these detectors is increasingly used for experiments at the SOLEIL synchrotron radiation facility. For example, feasibility tests for *in situ* determination of growing conditions of carpets of C nanotubes were performed on the Cristal beamline (ANR ALUCINAN reference: ANR-07-NANO-014). Figs. 15(*a*) and 15(*b*) present diffraction images obtained with, respectively, 580 µm and 45 µm carpet thickness in only 1 s exposure at 28 keV. Without any flat-field and geometric correction, diffraction rings with low intensity on the image shown in Fig. 15(*b*) are clearly visible. The high signal-to-noise ratio of the XPAD allows a high-fidelity reproduction of the incident diffraction pattern, being only limited by the Poisson fluctuations.

Having a four times better DQE at 28 keV, CdTe sensors will bring an additional benefit in terms of detection efficiency in such experiments. Three 2 cm × 3 cm CdTe detectors have been recently assembled. The detectors are based on two 1.5 cm × 2 cm Cdte sensors flip-chip bonded each on two circuits (Fig. 16*a*). Fig. 16(*b*) shows a first image taken with a

Figure 14
Silicon XPAD3S imager.

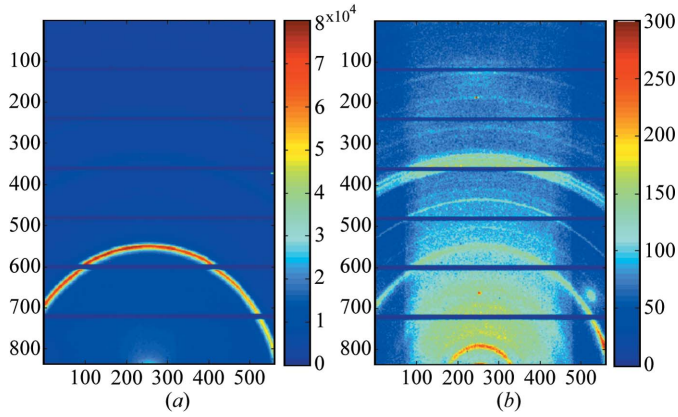

Figure 15
Diffraction on carpets of C nanotubes of (*a*) 580 µm and (*b*) 45 µm thickness. Images are not flat-field corrected and no geometric correction was used. The dark blue lines correspond to the shadow from the overlapping modules. The noise in the central part of the right-hand image originates from an extra Kapton window.

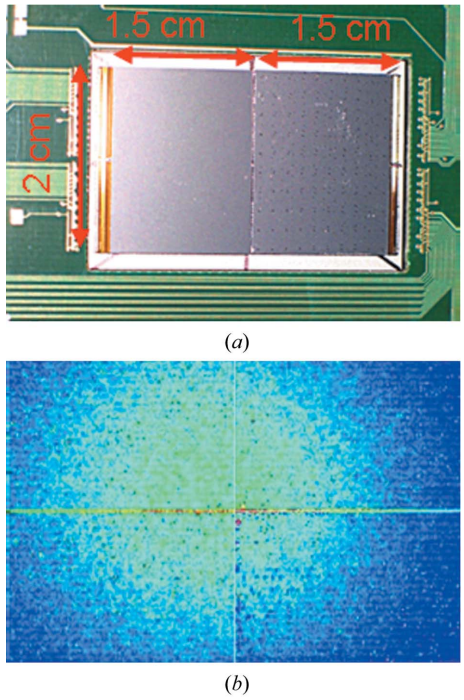

Figure 16
(*a*) 2 cm × 3 cm CdTe detector. (*b*) ^{241}Am (59 keV) source image.

^{241}Am (59 keV) source. The good bump-bonding yield of this large sensor is very promising.

7. Conclusion

Performance measurements have been carried out on the XPAD3 flip-chip bonded on 500 µm-thick Si and 700 µm-thick CdTe sensors. MTFs measured on both sensors at 26 keV are very similar and can be reasonably fit with the theoretical response obtained by the Fourier transform of a square aperture of width 130 µm. These results indicate that, with the XPAD pixel pitch and a threshold set at half of the energy of

the photons, the charge-sharing effect is very low. The spatial response on the CdTe sensor was investigated above the *K*-edge. A detailed study has demonstrated that the broadening of the spatial response observed is mainly produced by photon fluorescence emission. The induced tails on the LSF decrease the value of the MTF at the Nyquist frequency from 60% down to 40% which remains a good contrast transfer value. Therefore, with 130 µm pixel size, the effect of CdTe *K*-edges on spatial resolution is acceptable. This may not be the case for smaller pixel sizes, where the spatial response could become too poor above 26.8 keV.

The DQE at zero frequency was studied from 6 keV up to 35 keV. With the Si detector, it follows the absorption law whereas, with the CdTe sensor, a strong deficit at low photon energy was observed. It has been demonstrated that this effect is mainly produced by the existence of a 10 µm-thick inefficient layer below the anode contact. Nevertheless, even with this 'dead layer', the efficiency above 15 keV remains larger in CdTe compared with in Si.

Quad XPAD circuits with CdTe sensor have been successfully tested recently and will be soon characterized in terms of MTF, energy resolution and DQE as described in this paper. With these devices, further investigations will be conducted, in particular in order to clearly understand the cause of this 'dead layer' and to measure the pixel fill factor.

The large XPAD-Si imager is being used on SOLEIL beamlines for experiments and is giving very promising results. It confirms the necessity of this detector in studies of the following of the *in situ* growing of carpets of C nanotubes.

The next important step will be to evaluate the second version of the 'S' and 'C' circuit. On the fly readout, lower threshold dispersion, better energy resolution and both polarities for the 'C' version are expected.

We would like to thank the DIFFABS, PROXIMA1, CRISTAL and D2AM beamlines teams for their support on all experiments performed and we gratefully acknowledge Andy Thompson for his technical input to this manuscript.

References

Basolo, S., Bérar, J.-F., Boudet, N., Breugnon, P., Caillot, B., Clemens, J.-C., Delpierre, P., Dinkespiler, B., Hustache, S., Koudobine, I., Meessen, C., Menouni, M., Mouget, C., Palancher, H., Pangaud, P., Potheau, R. & Vigeolas, E. (2007). *J. Synchrotron Rad.* **14**, 151–157.

Basolo, S., Berar, J. F., Boudet, N., Breugnon, P., Chantepie, B., Clemens, J. C., Delpierre, P., Dinkespiler, B., Hustache, S., Medjoubi, K., Menouni, M., Morel, Ch., Pangaud, P. & Vigeolas, E. (2008). *Nucl. Instrum. Methods Phys. Res. A*, **589**, 268–274.

Bérar, J.-F., Blanquart, L., Boudet, N., Breugnon, P., Caillot, B., Clemens, J.-C., Delpierre, P., Koudobine, I., Mouget, C., Potheau, R. & Valin, I. (2002). *J. Appl. Cryst.* **35**, 471–476.

Berar, J. F., Boudet, N., Breugnon, P., Caillot, B., Chantepie, B., Clemens, J. C., Delpierre, P., Dinkespiller, B., Godiot, S., Meessen, Ch., Menouni, M., Morel, Ch., Pangaud, P., Vigeolas, E., Hustache, S. & Medjoubi, K. (2009). *Nucl. Instrum. Methods Phys. Res. A*, **607**, 233–235.

Bigas, M., Cabruja, E. & Lozano, M. (2007). *Nucl. Instrum. Methods Phys. Res. A*, **574**, 392–400.

Broennimann, Ch., Eikenberry, E. F., Henrich, B., Horisberger, R., Huelsen, G., Pohl, E., Schmitt, B., Schulze-Briese, C., Suzuki, M., Tomizaki, T., Toyokawa, H. & Wagner, A. (2006). *J. Synchrotron Rad.* **13**, 120–130.

Brönnimann, Ch., Eikenberry, E. F., Horisberger, R., Hülsen, G., Schmitt, B., Schulze-briese, C. & Tomizaki, T. (2003). *Nucl. Instrum. Methods Phys. Res. A*, **510**, 24–28.

Cassol Brunner, F., Clemens, J. C., Hemmer, C. & Morel, Ch. (2009). *Phys. Med. Biol.* **54**, 1773–1789.

Clajus, M., Cajipe, V. B., Hayakawa, S., Turner, T. O. & Willson, P. D. (2006). *IEEE Nucl. Sci. Symp. Conf. Rec.* **6**, 3602–3606.

Dainty, J. C. & Shaw, R. (1974). *Image Science: Principles, Analysis and Evaluation of Photographic Type Imaging Processes.* New York: Academic Press.

Delpierre, P., Basolo, S., Berar, J. F., Bordesoule, M., Boudet, N., Breugnon, P., Caillot, B., Chantepie, B., Clemens, J. C., Dinkespiler, B., Hustache-Ottini, S., Meessen, C., Menouni, M., Morel, C., Mouget, C., Pangaud, P., Potheau, R. & Vigeolas, E. (2007). *Nucl. Instrum. Methods Phys. Res. A*, **572**, 250–253.

Ejdrup, T., Lemke, H. T., Haldrup, K., Nielsen, T. N., Arms, D. A., Walko, D. A., Miceli, A., Landahl, E. C., Dufresne, E. M. & Nielsen, M. M. (2009). *J. Synchrotron Rad.* **16**, 387–390.

Fröjdh, C., Graafsma, H., Nilsson, H. E. & Ponchut, C. (2006). *Nucl. Instrum. Methods Phys. Res. A*, **563**, 128–132.

Henrich, B., Bergamaschi, A., Broennimann, C., Dinapoli, R., Eikenberry, E. F., Johnson, I., Kobas, M., Kraft, P., Mozzanica, A. & Schmitt, B. (2009). *Nucl. Instrum. Methods Phys. Res. A*, **607**, 247–249.

Katz, L. & Penfold, A. S. (1952). *Rev. Mod. Phys.* **24**, 28–44.

Matsumoto, C., Takahashi, T., Takizawa, K., Ohno, R., Ozaki, T. & Mori, K. (1998). *IEEE Trans. Nucl. Sci.* **45**, 428–432.

Pangaud, P., Basolo, S., Boudet, N., Berar, J. F., Chantepie, B., Clemens, J. C., Delpierre, P., Dinkespiler, B., Medjoubi, K., Hustache, S., Menouni, M. & Morel, Ch. (2008). *Nucl. Instrum. Methods Phys. Res. A*, **591**, 159–162.

Pangaud, P., Basolo, S., Chantepie, B., Clemens, J. C., Delpierre, P., Dinkespiler, B., Menouni, M., Bonissent, A., Debarbieux, F. & Morel, Ch. (2007). *IEEE Nucl. Sci. Symp. Conf. Rec.* **1**, 14–18.

Ponchut, C. (2006). *J. Synchrotron Rad.* **13**, 195–203.

Ponchut, C., Clement, J., Rigal, J. M., Papillon, E., Vallerga, J., Lamarra, D. & Mikulec, B. (2007). *Nucl. Instrum. Methods Phys. Res. A*, **576**, 109–112.

Ponchut, C., Zontone, F. & Graafsma, H. (2005). *IEEE Trans. Nucl. Sci.* **52**, 1760–1765.

Spieler, H. (2008). *Semiconductor Detector Systems.* Oxford Science Publications.

Toyama, H., Higa, A, Yamazato, M., Maehama, T., Ohno, R. & Toguchi, M. (2006). *Jpn. J. Appl. Phys.* **45**, 8842–8847.

Zahraman, K., Roumie, M., Raulo, A., Auricchio, N., Ayoub, M., Donati, A., Dusi, W., Hage-Ali, M., Lmaï, F., Perillo, E., Siffert, P., Sowinska, M. & Ventura, G. (2006). *IEEE Trans. Nucl. Sci.* **53**, 378–382.

Zwerger, A., Fauler, A., Fiederle, M. & Jakobs, K. (2007). *Nucl. Instrum. Methods Phys. Res. A*, **576**, 23–26.